b-value variations and fracture pinning

J. Schmittbuhl[1], A. Stormo[1], O. Lengliné[1], C. Justin[1] and A. Hansen[2].

[1] EOST, Strasbourg University/CNRS Company, 5 rue René Descartes, 67084 Strasbourg France

[2] Department of Physics, NTNU,Trondheim, Norway

Jean.Schmittbuhl@unistra.fr

Keywords: Microseismicity; b-value; Fiber bundle model, interfacial crack, asperity pinning, self-affine roughness, local crack velocity.

ABSTRACT

We propose to interpret possible fluctuations of the b-value on the basis of a simple fault model. It relies on the observation that many deep reservoirs host only a very limited number of major faults, e.g. in Soultz-sous-Forêts, Alsace, where most of the induced seismicity is related to one major fault. Our numerical model consists of a weak and fragile fault with a discrete set of asperities embedded in a stiff elastic matrix on which the fracture front intermittently pins and depins. Depinning periods are related to bursts that are considered as analogues of micro-seismic events. We show that the relative stiffness of the fault with respect to that of the matrix is the key parameter which controls the development of two different regimes of b-values of the magnitude distribution of these events.

1. INTRODUCTION

The distribution of earthquake magnitudes is a classical tool for monitoring induced seismicity in deep geothermal reservoirs. One of the most classical measurement is its b-value. Indeed, earthquakes recorded worldwide from various natural fault environments exhibit a specific magnitude distribution. This distribution is well represented by the Gutenberg-Richter empirical law which states that:

$$\log 10\ N(M) = a - bM, \qquad [1]$$

where N(M) is the number of events with a magnitude greater or equal to the magnitude M, and a and b are the parameters that are inverted from the earthquake magnitude dataset [Gutenberg and Richter (1944)]. The parameter a scales with the number of earthquakes in the investigated catalog while the parameter b, b-value, is an exponent which quantifies the overall proportion between larger and smaller magnitude events in the earthquake catalog. It is typically considered as universal but still shows important fluctuations through time and space during reservoir stimulations. Despite being often related to statistical issues and being a very crude information i.e. a scalar average of a very complex mechanical stress evolution, these variations are expected to provide insights about the mechanics of the reservoir.

While generally close to b = 1.0, e.g., Schorlemmer et al. (2005) and Kwiatek et al. (2010), several variations of the b value are also noticed, e.g., Schorlemmer et al. (2005), Enescu and Ito (2001), and Amitrano (2003). These fluctuations attest for a possible physical control on the value of this exponent and its observed fluctuations.

Apart from natural systems and laboratory experiments, the Gutenberg-Richter distribution of earthquakes is also observed for induced seismicity. One example of the later is the case of the stimulation of deep geothermal reservoir. Indeed, for the development of deep geothermal reservoirs (Enhanced Geothermal Systems (EGS)) like at Soultz-sous Forêts, France [Dorbath et al. (2009)] or Basel, Switzerland [Bachmann et al. (2011)], hydraulic injections have been used to stimulate the existing fracture network both in the sediments and in the granite massif in order to enhance the permeability of the reservoir.

For instance, during the hydraulic injection of the Soultz-sous-Forêts GPK2 well in 2000, a significant seismic activity was generated, mapping the development of the fault network [Cuenot et al. (2008)]. Up to 30,000 earthquakes were recorded with a magnitude ranging from−0.9 to 2.6. Earthquake magnitude distribution was found to follow the typical Gutenberg-Richter distribution. During the 2000 injection, the b-value wasmeasured to be 1.29 for the entire period [Cuenot et al. (2008)]. However, when searching for temporal variations, the b-value was observed to evolve from 1.0 to 1.7. High injection rates led to higher b-value. Similar variations of the b-value during injection were observed in Basel during the 2006 experiment. During the injection, b-value was measured to be 1.58 but lowered to 1.15 after shut-in [Bachmann et al. (2011)]. These temporal and spatial fluctuations of the b-value suggest to use this information as a tracer of the evolution of the reservoir (in the case of induced seismicity) or the fault system (in natural environment).

Numerous models have been proposed to explain the variability of the b-value. One of the first model is a theoretical study of rock fracture developed by Scholz (1968). This model was based on a heterogeneous distribution of material strength in a sample under load. It was found that the b-value is a function of the applied stress, and that the frequency of fracture size was scale free. Similar results were obtained by Wyss (1973) suggesting that low b-values correlate with high stresses. Although these models bring a possible explanation of the observed b-value fluctuations, some care should be taken when interpreting stress from the b-value alone since it is a scalar quantity that cannot characterize completely the stress tensor. Many other models concerning the connection between earthquakes and micro-fractures have been developed through the years in the language of statistical physics, e.g., Holliday et al. (2008). In particular, approaches that connect fiber-bundle models to acoustic emissions during rock fracturing have been done [Turcotte et al. (2003); Pradhan et al. (2010)]. For an overlook of this particular field, we refer to the review by Rundle et al. (2003).

Several attempts have also been made in order to model the b-value and its fluctuations specifically for induced seismicity in geothermal system, e.g., Hakimhashemi et al. (2014). Baisch et al. (2010) considered a single fault to model the induced seismicity at Soultz-sous-Forêts. They indeed noticed that hypocenters are aligned along a pre-existing planar fault structure which concentrates most of the recorded seismicity. Their quasi-static model includes sliders connected by springs that incorporate elastic stress redistribution. The effect of fluid is simply modelled as a change of pore pressure bringing each path of the model closer to failure in the Mohr-Coulomb sense. Based on this simple model, they reproduced most of the seismicity characteristics: migration of the seismicity,

It then appears that many different models from very different physical mechanisms are able to reproduce the frequency magnitude distribution of the seismicity in EGS reservoirs. It therefore questions about how to interpret the change of b-values in the light of so different modelling. We decided here to study another aspect: the evolution of damage and its link with seismic events considering only a quasi-static model, where damages are represented on a single fault plane and where the fluid source is not explicitly modelled. Although our approach is oversimplified compared to the rich complexity of induced seismicity of geothermal system, it allows us to test the direct influence of several parameters such as the stiffness of the system. Our model is inspired by the model developed by Stormo et al, (2015), (2016). We focus on the analysis of burst distributions. We notably explore the impact of the definition of the event in the results of the frequency magnitude distribution. We indeed introduced a new definition of a burst based on the local velocity of the crack front propagation. We show that this definition provides an interesting perspective for comparison with large scale fluctuations of the b-values.

2. NUMERICAL MODEL

Our model is a variation of the fiber bundle model, i.e., a model of a single fracture described as an interfacial failure along a discrete set of connecting fibers. We assume that the fault network in the geothermal reservoir is dominated by a discrete set of pre-existing faults as it was shown by Sausse et al. (2010) at Soultz-sous-Forêts.We even push further the hypothesis and reduce the fault network for seismicity modelling to a single main fault zone as previously proposed by Baisch et al. (2010). The response of the main fault is seen as a collection of weak fibers attached to the fault boundaries displaced apart by a distance D because of hydraulic pressure increase. Our variation of the fiber bundle model is to deal with the elastic fiber bundle model, first proposed by Batrouni et al. (2002). It is an attempt to include non-local elastic mechanics to the fiber bundle models by replacing the rigid boundaries of the global load sharing configuration by deformable elastic half-spaces. Actually, this configuration of two facing elastic half-spaces is equivalent to a single elastic half-space with equivalent elastic moduli facing a rigid block as discussed in Batrouni et al. (2002). Variability of the fracture aperture could have been introduced by considering a specific morphology of the rigid part as proposed in Stormo et al. (2016). However, we consider the presence of a static fluid in the fracture by dealing with normal effective stresses on the fibers but neglect other specific fluid effects like viscous pressure or dynamic effects [Jaeger et al. (2009)].

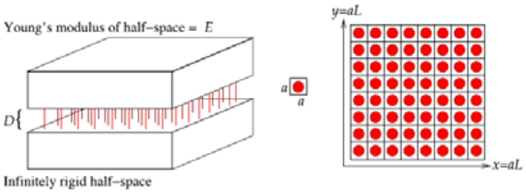

Figure 1 Setup of the elastic fiber bundle model. On the left, a sketch of the fiber bundle. The upper half-space deflects in response to the forces applied by the fibers (red), while the infinitely rigid lower half-space is displaced downward of a distance D . To the right, a schematic top view of the entire fiber bundle where each red circle represents a fiber at the center of a mesh of size a × a.

The soft clamp fiber bundle model was used in order to reproduce the phenomena occurring at the process zone scale around the fracture front by introducing the appropriate boundary conditions. We are indeed interested in describing the behavior of the fracture front on a short range from its edge. We thus consider our model as a square of dimension $Lf \times Lf$ around the fracture front. This area of the system is illustrated in Figure1 by the dark square covering apart of the fracture front. This area is divided into $N \times N$ sub-squares, each of them containing a single fiber. A discretization size is then $dl = Lf/N$. The two facing plates are represented as infinite facing half-spaces, and act as clamps attached to the N^2 fibers. The half spaces are supposed to have an elastic behavior with a Young modulus E and a Poisson ratio of ν. An equivalent simpler configuration can be obtained by assuming that one of the half spaces is infinitely stiff. Thus, E will only describe the elastic response of the other half-space. The system is periodic along the *x*-axis. Details of the modeling can be found in Stormo et al, (2015).

During the computation of the crack front advance, the system is updated iteratively and quasistatically by removing the fibers one by one following an event-driven algorithm [Schmittbuhl et al, (1995)]. At each step we compute a new prefactor D_0 that will correspond to a force field where only one of the fibers is experiencing a force equal to its strength threshold. This fiber is actually the closest one to failure and thus requires the least increase of D_0 to break. The fiber is then removed and the procedure is continued until there is no intact fiber left.

When the distances are measured in units of the discretization size dl, the relative influence of the elastic interactions with respect to the global loading has been found to be described by a single parameter named the reduced Young modulus [Stormo et al, 2012]:

$$e = E\,dl/N \qquad [2]$$

where E is the Young modulus, N the number of fibers per system length L_f . Indeed, the contribution of the Green function in the force computation of each fiber can be turned on or off, depending on the value e. In the stiff regime, i.e., large e, the fracture process is dominated by a diffusive damage controlled by the strength heterogeneities in the system. When e decreases, the system goes through a cross-over regime where the influence of the elastic forces rises. When e is sufficiently low, the competition between the elastic redistribution and the strength heterogeneities are balanced and the system enters a so-called soft regime. This regime is dominated by localized damage. As we can see from Equation (2), decreasing E, while increasing N in a way that keeps e constant is not affecting the influence of the Green function. We will thus associate the soft systems with large length scales. Similarly, we will associate the stiff systems with short length scales.

To better capture the physical meaning of the controlling parameter e, it is of interest to rewrite e as: $e = dl^2/L_f^2 \cdot L_f \cdot E$ which reads as: $e = L_f \cdot E/N^2$ where N^2 is the number of fibers in the system. If one has in mind that $L_f \cdot E$ is the effective stiffness of the elastic medium and $N \cdot 1$ is the effective stiffness of the set of fibers in parallel (when they are all present and considering a unit stiffness of each fiber), one realizes that e is the ratio of the stiffness of the bulk to the stiffness of the interface: $e = L_f \cdot E/(N^2 k_f)$ with k_f the stiffness of each fiber. The controlling parameter is then the dimensionless ratio of the two stiffnesses: that of the bulk to that of the interface. When the bulk is very stiff compared to the interface (large e), everything is dominated by the elastic bulk and when the interface is very stiff compared to the bulk, one has a so called soft system.

4. ANALOGICAL MODEL

We compare our numerical results to experimental results obtained with the following setup. It consists of two transparent welded plexiglas (PMMA - poly methyl methacrylate) plates [e.g., Schmittbuhl et al (1997), Delaplace et al, (1999), Maloy et al, (2001), Lengliné et al, (2011)]. Disorder in the strength of the interface between the two plates is introduced by sandblasting using glass beads of variable diameters (180–300 μm), the opposite surfaces of the two plates that are to be welded together. Welding of the two plates is then achieved by imposing a normal load on the assembled plates while heating the system at 190◦C. This thermal annealing produces a cohesive interface weaker than the bulk, along which the sample will break apart under normal opening loading. When the system is loaded from one side, a propagating crack evolves and moves away from the loaded side. We are focusing upon this crack front.

The dimensions are typically 20 cm long, 3 cm wide and 5 mm thick for the bottom plexiglas plate and 1 cm thick for the upper plate. The upper plate is attached to a stiff aluminum frame while a load is applied over the top side of the bottom plate in a direction normal to the plate interface. The vertical displacement imposed on the bottom plate induces stable mode I propagation of a planar fracture along the prescribed weak interface (mode II and III components related to the finite size of the sample and friction along the loading rod are neglected). A sketch of the experiment is given in Figure 2.

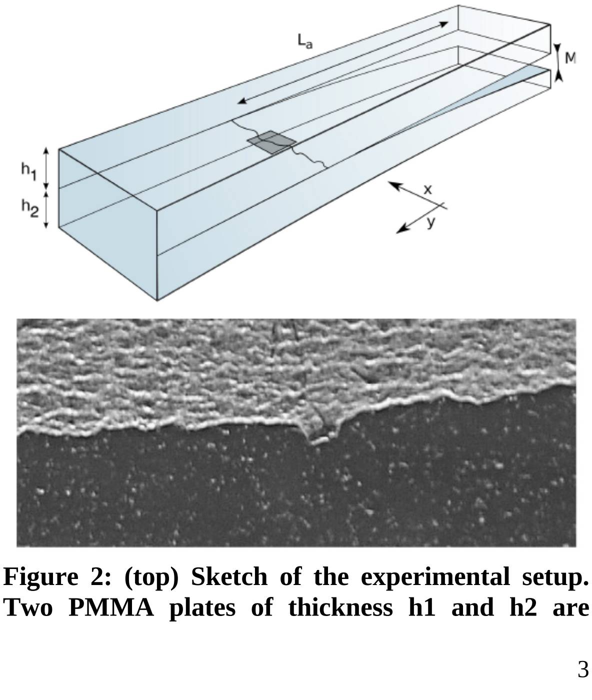

Figure 2: (top) Sketch of the experimental setup. Two PMMA plates of thickness h1 and h2 are

welded and a mode I fracture propagates at the interface between the two plates. Fracture propagation is caused by the opening, M, between the two plates. The distance between the loading point and the crack front is noted La. The crack front propagates along the y direction. The grey rectangle marks the area around the crack front (see bottom) we will reproduce in our simulations. (bottom) Picture of the crack front area obtained during an experiment. The crack is propagating from top to bottom, the grey part refers to already broken part and the dark area to the unbroken part. The optical contrast between this two parts defines the fracture front. The dimension of the picture in the x-direction is 4 mm

The fracture front creates an optical contrast between the broken and unbroken sections of the interface [Delaplace et al, (1999)]. This fracture front is then tracked by an optical digital camera (a Nikon D700 with a resolution of 4256×2832 pixels at up to 5 images/s for slow monotoring or an Optronis Camrecord 600 with a resolution of 1000 × 1000 pixels at 1000 images/s for fast tracking) in order to extract its position through time [Lengliné et al, (2011a), (2011b), (2012)]. The front propagates along the y axis where the origin is defined at the loading point and is positive in the direction of crack propagation (see Figure 2). The x axis is perpendicular to y and defines the coordinate of a point along the front. The large scale bending of the plate at the sample size is well reproduced by the elastic beam theory [Lengliné et al, (2011a)]. At a smaller scale i.e., at the scale of the process zone, the elastic beam theory might however not be any more valid in describing the shape of the plate and typical crack solutions eventually provide more a realistic description as discussed below.

5. LOCAL CRACK FRONT VELOCITIES

A direct way for studying the dynamics of the fracture propagation is to measure the distribution of the local velocity along the crack front. To obtain this we use the waiting time matrix technique developed by Måløy et al. (2006), on experimental data. The waiting time matrix W gives at each sub-squared (i.e., pixel), the time spent by the crack front at this location. This waiting time is measured in our simulations, by identifying the fracture front at each time step (i.e., each broken fiber) and increasing each element of W covered by the crack front by one. After doing this for the entire fracture propagation, we obtain the final estimate of W. From W, we can create the velocity matrix V. Each element of V is indeed the inverse element of W times the discretization length dl1. This creates a map of the local velocities of the fracture front. Examples of velocity maps are given in Figure 3 for both regimes together with a map at two scales from experimental measurements [Lengliné et al, 2012]. It provides a direct visual observation of the pinning of the crack front in our simulation. Comparisons with experimental data show a good agreement and confirm that the stiff regime describes the details of the propagation at small scales and the soft regime at large scales.

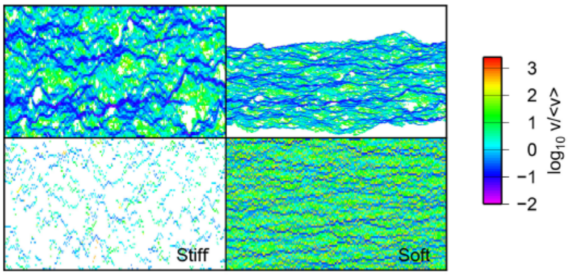

Figure 3: Comparison of the local normalized velocity maps obtained for an experiment at two scales (top): at large scale (top right), and a detail at small scale (top left); and two simulations: in the soft regime (bottom right) and in the stiff regime (bottom left) (bottom). White dots correspond to areas where the local velocity was not measurable, i.e., too fast for the local waiting time method.

6. BRITTLE/DUCTILE TRANSITION

There are several ways to define the difference between ductile and brittle damage. Just as Amitrano (2003), we will use the amount of inelastic, i.e., the non-linear deformation the system sustains before critical damage occurs as a measure of ductility. If there is instead a strongly linear load-displacement all the way until failure, we name it a brittle system. We then study the load-displacement curves from the stiff (e = 32) and soft (e = 7.63 · 10−6) systems shown in Figure 4. On top, we can see the load-displacement for stiff systems. The load is defined as the global stress Σ, and calculated as the sum of force applied on the fibers divided by the area of the system. It is clear that the load-displacement curve is highly non-linear until critical damage (indicated by the star). This corresponds to our definition of ductility. On the bottom, we see the same curve for a soft system. In contrast to the stiff system, there seems to be no sign of non-linear deformation before failure (indicated by the star). Thus, we have a strong indication of a ductile to brittle transition as we move from the stiff regime to the soft one.

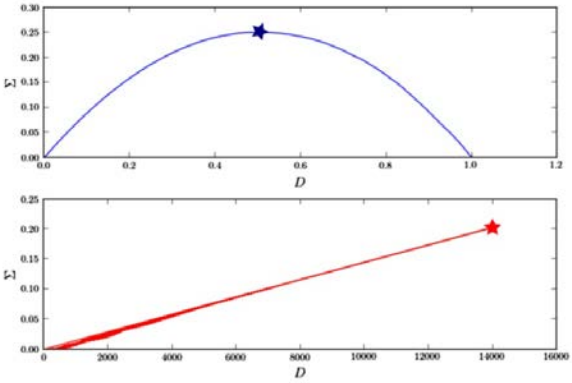

Figure 4: The load Σ as a function of displacement D. Top: Load displacement for stiff, ductile systems (e = 32). Bottom: Load displacement for soft,

brittle systems ($e = 7.63 \cdot 10^{-6}$). The point of critical damage is indicated by a star.

7. DAMAGE BURST DISTRIBUTION

We introduce the definition of burst that is typically employed in quasi-static models in order to compare quasi-static time p to laboratory time. It is assumed that during a simulation, if a fiber breaks and the resulting load redistribution induces more fibers exceeding their force threshold f^t, then the latter fibers are also damaged at the same time. Following the Σ(n)-curve in Figure 5, we can see local maxima where the subsequent fibers fail at a lower load. In laboratory time, we assume the number of fibers:

$$\delta = \Delta n, \qquad [3]$$

that break before Σ is increased, fail in an avalanche or burst. In order to compare our model to the one presented by Amitrano (2003), we want to find the distribution of temporal damage bursts. We can then extract a burst distribution exponent b-value from our system using the event-size distribution. We recall from Equation 8 that we define the size of an event δ as the number of fibers that are broken for each increase of the load Σ. In Figure 5, we see a zoomed version of Σ (p), and we can identify δ. Burst data ends at pc, as it is the point of maximum Σ. Following Amitrano (2003), we assume that the size of events are comparable to the magnitude of acoustic emissions, and we thus get the δ-b connection:

$$\log10[N(\delta)] \propto -b \log10[\delta]\ , \qquad [4]$$

where N(δ) is the number of bursts of size δ or higher. We run the elastic fiber-bundle model for both the stiff (e = 32) regime with diffuse ductile failure, and the soft (e = 7.63 · 10−6) regime with localized brittle failure. This is done for both regimes at L =[32, 64, 128, 256].

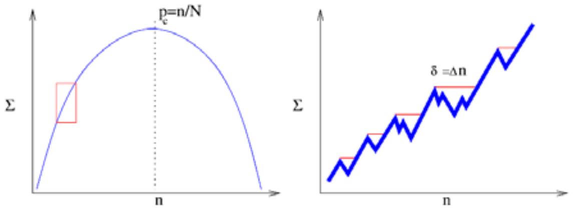

Figure 5: Typical load-displacement curve. Left: Typical Σ (n) force evolution with 'time' (i.e., number of broken fibers) in the elastic fiber bundle. Right: Zoom of force evolution indicated by the red area. Burst sizes δ are defined as the number of fibers broken before an increase of global load Σ is obtained. They are illustrated by horizontal red lines.

For stiff systems, we obtain the slope of 1.475 for the linear trend for δ/Lγ ≤ 1 for the burst distribution which is consistent with the theoretical 1.5 burst exponent for the equal load sharing fiber bundle model [see Pradhan et al. (2010), Stormo et al. (2015)]. This gives us a size-independent stiff b-value of 1.475 for L =[32, 64, 128, 256].We also observe a good collapse of the data for the different size systems using the collapsing method of Girard et al. (2010) and obtained similar values of γ = 1.2 and α = 1.6.

In contrast from the stiff systems, the soft systems have size-dependent b-values [Stormo et al, (2015)]. The slope of the burst distribution gives b(L) =[2.02, 2.23, 2.60, 3.00] for L =[32, 64, 128, 256], with no clear sign of convergence. As changing L also influences the elastic behavior of the system from Equation 2, we tested the sole influence of e on the slope of the burst distribution, keeping L constant and taking L = 64 (see Figure 6).

Results obtained in these simulations are less precise that those obtained for e = 32 and e = 7.63 · 10−6, but they highlight that the slope is controlled by the value of e. At high e the slope reaches the value 1.475 independently of e as observed previously while the b-value goes to higher values as e decreases. It confirms that e ≈ 10−2 is at the transition between both regimes.

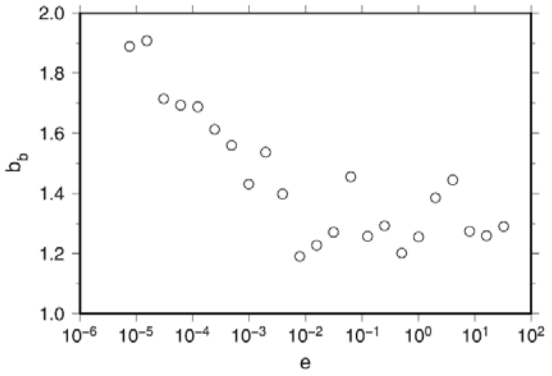

Figure 6: b-values obtained from the slope of the cumulative distribution of damage burst sizes for various e moduli. The system size is set to L = 64. Each point is an average over 400 simulations.

3. CONCLUSIONS

We have found that the elastic fiber bundle model shows promising features to understand the mechanical origin of the b-value fluctuations during stimulation of deep geothermal reservoirs. We proposed that damage bursts in our model that can be compared to seismic events. The damage event distribution has a b-value that is influenced by the normalized e modulus: changing at small e (soft systems) but constant at large e (stiff systems). We show that the e-modulus is related to the relative stiffness of the fault with respect to that of the matrix. It is the key parameter which controls the development of two different regimes of b-values. When the fault is submitted to a normal loading produced by the hydraulic stimulation, the magnitude distribution of the failures of the asperities shows significant b-value changes: from large b-values to low b-values as the relative stiffness of the bulk is decreased with respect to the stiffness of the average fault asperities. We checked from close comparisons with experimental results of interfacial crack propagation that the model is valid. Finaly, we conclude that the proposed model is a new and interesting framework for interpreting b-value changes during deep reservoir stimulations.

REFERENCES

Amitrano D (2003) Brittle-ductile transition and associated seismicity: experimental and numerical studies and relationship with the b value. J Geophys Res Earth 1978–2012 108(B1):2044

Bachmann CE, Wiemer S, Woessner J, Hainzl S (2011) Statistical analysis of the induced Basel 2006 earthquake sequence introducing a probability-based monitoring approach for enhanced geothermal systems. Geophys J Int 186(2):793–807

Baisch S, Vörös R, Rothert E, Stang H, Jung R, Schellschmidt R (2010) A numerical model for fluid injection induced seismicity at Soultz-sous-Forêts. Int J Rock Mech Mining Sci 47(3):405–413

Batrouni GG, Hansen A, Schmittbuhl J (2002) Heterogeneous interfacial failure between two elastic blocks. Phys Rev E, 65(3):036126

Cuenot N, Dorbath C, Dorbath L (2008) Analysis of the microseismicity induced by fluid injections at the EGS site of Soultz-sous-Forêts (Alsace, France): implications for the characterization of the geothermal reservoir properties. Pure Appl Geophys 165(5):797–828

Delaplace A, Schmittbuhl J, Måløy KJ. High resolution description of a crack front in an heterogeneous plexiglas block. Phys Rev E (1999) 60:1337–43. doi: 10.1103/PhysRevE.60.1337

Dorbath L, Cuenot N, Genter A, Frogneux M (2009) Seismic response of the fractured and faulted granite of Soultz-sous-Forêts (France) to 5 km deep massive water injections. Geophys J Int 177(2):653–675

Enescu B, Ito K (2001) Some premonitory phenomena of the 1995 Hyogo-Ken Nanbu (Kobe) earthquake: seismicity, b-value and fractal dimension. Tectonophysics 338(3):297–314

Gutenberg B, Richter CF (1944) Frequency of earthquakes in California. Bull Seismological Soc Am 34(4):185–188

Hakimhashemi AH, Yoon JS, Heidbach O, Zang A, Grünthal G (2014) Forward induced seismic hazard assessment: application to a synthetic seismicity catalogue from hydraulic stimulation modelling. J Seismol 18(3):671–680

Holliday JR, Turcotte DL, Rundle JB (2008) A review of earthquake statistics: fault and seismicity-based models, ETAS and BASS. Pure Appl Geophys 165(6):1003–1024

Kwiatek G, Plenkers K, Nakatani M, Yabe Y, Dresen G, JAGUARS Group (2010) Frequency-magnitude characteristics down to magnitude-4.4 for induced seismicity recorded at Mponeng Gold Mine, South Africa. Bull Seismological Soc Am 100(3):1165–1173

Lengliné O, Toussaint R, Schmittbuhl J, Elkhoury JE, Ampuero JP, Tallakstad KT, et al. Average crack-front velocity during subcritical fracture propagation in a heterogeneous medium. Phys Rev E (2011)a 84:036104. doi: 10.1103/PhysRevE.84.036104

Lengliné O, Schmittbuhl J, Elkhoury JE, Ampuero JP, Toussaint R, Måløy KJ. Down-scaling of the fracture energy during brittle creep experiments. (2011)b J Geophys Res. 116:B08215. doi: 10.1029/2010JB008059

Lengliné O, Elkhoury JE, Daniel G, Schmittbuhl J, Toussaint R, Ampuero JP, et al. Interplay of seismic and aseismic deformations during earthquake swarms: an experimental approach. Earth Planet Sci Lett. (2012) 331–332:215–23. doi: 10.1016/j.epsl.2012.03.022

Måløy KJ, Santucci S, Schmittbuhl J, Toussaint R. Local waiting time fluctuations along a randomly pinned crack front. Phys Rev Lett. (2006) 96:045501. doi: 10.1103/PhysRevLett.96.045501

Måløy KJ, Schmittbuhl J. Dynamical events during slow crack propagation. Phys Rev Lett. (2001) 87:105502. doi: 10.1103/PhysRevLett.87.105502

Pradhan S, Hansen A, Chakrabarti BK (2010) Failure processes in elastic fiber bundles. Rev Modern Phys, 82(1):499

Rundle JB, Turcotte DL, Shcherbakov R, Klein W, Sammis C (2003) Statistical physics approach to understanding the multiscale dynamics of earthquake fault systems. Rev Geophys 41(4):1019

Sausse J, Dezayes C, Dorbath L, Genter A, Place J (2010) 3D model of fracture zones at Soultz-sous-Forêts based on geological data, image logs, induced microseismicity and vertical seismic profiles. Comptes Rendus Geosciences, 342(7):531–545

Schmittbuhl J, Måløy KJ. Direct observation of a self-affine crack propagation. Phys Rev Lett. (1997) 78:3888. doi: 10.1103/PhysRevLett. 78.3888

Scholz CH (1968) The frequency-magnitude relation of microfracturing in rock and its relation to earthquakes. Bull Seismological Soc Am 58(1):399–415

Schorlemmer D, Wiemer S, Wyss M (2005) Variations in earthquake-size distribution across different stress regimes. Nature 437(7058):539–542

Stormo A, Gjerden KJ, Hansen A., Onset of localization in heterogeneous interfacial failure. Phys Rev E (2012) 86:025101. doi: 10.1103/PhysRevE.86.025101

Stormo A, O. Lengliné and J. Schmittbuhl., (2015), Mechanical origin of b-value changes during stimulation of deep geothermal reservoirs Geothermal Energy, 3:1, DOI 10.1186/s40517-014-0022-0

Stormo, A., Lengliné, O., Schmittbuhl, J., and Hansen, A. (2016) Soft-Clamp Fiber Bundle Model and Interfacial Crack Propagation: Comparison Using a Non-linear Imposed Displacement., Front.Phys.4:18, doi: 10.3389/fphy.2016.00018.

Turcotte DL, Newman WI, Shcherbakov R (2003) Micro and macroscopic models of rock fracture. Geophys J Int 152(3):718–728

Wyss M (1973) Towards a physical understanding of the earthquake frequency distribution. Geophys J R Astronomical Soc 31(4):341–359

Acknowledgements

We acknowledge support from ANR SUPNAF, Labex G-EAU-THERMIE PROFONDE (grant no. ANR-11-LABX-0050) and the Norwegian Research Council through grant no. 1999770.